Origin of Interstitial Doping Induced Coercive Field Reduction in Ferroelectric Hafnia

Tianyuan Zhu,[1,2,*] Liyang Ma,[1,*] Xu Duan,[3] Shiqing Deng,[4] and Shi Liu[1,2,†]

[1]*Department of Physics, School of Science, Westlake University, Hangzhou, Zhejiang 310030, China*
[2]*Institute of Natural Sciences, Westlake Institute for Advanced Study, Hangzhou, Zhejiang 310024, China*
[3]*School of Science, Zhejiang University of Science and Technology, Hangzhou, Zhejiang 310023, China*
[4]*Beijing Advanced Innovation Center for Materials Genome Engineering, University of Science and Technology Beijing, Beijing 100083, China*

(Received 3 July 2024; revised 9 December 2024; accepted 24 December 2024; published 4 February 2025)

Hafnia-based ferroelectrics hold promise for nonvolatile ferroelectric memory devices. However, the high coercive field required for polarization switching remains a prime obstacle to their practical applications. A notable reduction in coercive field has been achieved in ferroelectric $Hf(Zr)_{1+x}O_2$ films with interstitial Hf(Zr) dopants [Science **381**, 558 (2023)], suggesting a less-explored strategy for coercive field optimization. Supported by density functional theory calculations, we demonstrate the $Pca2_1$ phase, with a moderate concentration of interstitial Hf dopants, serves as a minimal model to explain the experimental observations, rather than the originally assumed rhombohedral phase. Large-scale deep potential molecular dynamics simulations suggest that interstitial defects promote the polarization reversal by facilitating $Pbcn$-like mobile 180° domain walls. A simple prepoling treatment could reduce the switching field to less than 1 MV/cm and enable switching on a subnanosecond timescale. High-throughput calculations reveal a negative correlation between the switching barrier and dopant size and identify a few promising interstitial dopants for coercive field reduction.

DOI: 10.1103/PhysRevLett.134.056802

Ferroelectric hafnia (HfO_2) has emerged as a promising candidate for integrating ferroelectric functionalities into integrated circuits, enabled by its robust spontaneous polarization and exceptional silicon compatibility [1–3]. However, the high coercive field ($\mathcal{E}_c$) required to switch the polarization in HfO_2-based thin films remains a critical issue, impeding the commercialization of this silicon-compatible ferroelectric [3,4]. Typically, polycrystalline thin films of hafnia fabricated through atomic-layer deposition display an $\mathcal{E}_c$ exceeding 1 MV/cm [5]. High-quality epitaxial thin films, obtained by pulsed laser deposition, can show even higher $\mathcal{E}_c$ values of ≈2–5 MV/cm [6–9]. The need for applying high electric fields, close to the material's breakdown strength, for polarization reversal seriously limits its field cycling endurance. Reducing $\mathcal{E}_c$ without sacrificing the ferroelectricity of hafnia is a pressing challenge for the wider adoption of HfO_2-based ferroelectrics.

Various strategies such as doping [10,11], strain [12,13], and superlattices [14] have been theoretically explored to lower the barrier for polarization switching, aiming to reduce $\mathcal{E}_c$. Investigations based on density functional theory (DFT) revealed that the polarization switching process in the ferroelectric orthorhombic (O) $Pca2_1$ phase often involves an intermediate tetragonal (T) $P4_2/nmc$ phase, and the energy difference between these two phases could serve as a measure of the switching barrier [11,15]. Substitutional Si has been suggested as an effective dopant for reducing $\mathcal{E}_c$ due to its intrinsic sp^3 bonding with oxygen, which helps stabilize the intermediate T phase [11,16]. Conversely, most other substitutional dopants have shown limited effectiveness in influencing $\mathcal{E}_c$ based on DFT calculations [11]. Recently, a substantial reduction in $\mathcal{E}_c$, down to ≈0.65 MV/cm, has been achieved in thin films of $Hf(Zr)_{1+x}O_2$, a composition rich in hafnium-zirconium [Hf(Zr)] [17]. This reduction was attributed to the interstitial doping of Hf and Zr atoms into a polar rhombohedral (R) $R3m$ phase. DFT calculations show that a 7%-strained R-phase $Hf_{1.08}O_2$ exhibits a switching barrier of 7.6 meV/atom, significantly lower than that of 20 meV/atom in stoichiometric R-HfO_2.

However, assuming a polar R phase in $Hf_{1.08}O_2$ films grown via magnetron sputtering leads to notable discrepancies between theory and experiment [18,19]. The unstrained R phase is actually a nonpolar cubic $P\bar{4}3m$ phase [3,20]; the polar $R3m$ symmetry only emerges under an equibiaxial compressive strain within the (111) crystallographic plane. Although the relative stability between the R and O phases can be reversed with 8% interstitial doping [17], highly doped R-$Hf_{1.08}O_2$ without strain remains nonpolar; a giant tensile strain of 7% along the out-of-plane direction is nevertheless required to induce a polarization of ≈15 μC/cm², still below the experimental value of 22 μC/cm² in polycrystalline films [17].

*These authors contributed equally to this work.
†Contact author: liushi@westlake.edu.cn

 © 2025 American Physical Society

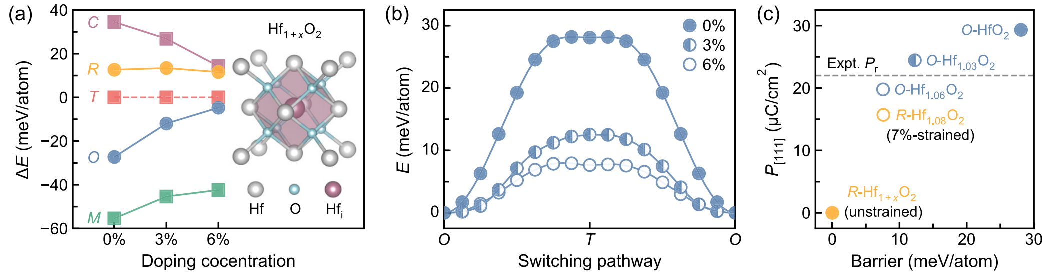

FIG. 1. Phase stability and ferroelectric switching of $Hf_{1+x}O_2$. (a) Energy landscape of monoclinic (M) $P2_1/c$, orthorhombic (O) $Pca2_1$, tetragonal (T) $P4_2/nmc$, rhombohedral (R) $R3m$, and cubic (C) $Fm\bar{3}m$ phases under interstitial doping at different concentrations (3% and 6%, short for 3.125% and 6.25%, respectively). The energy of the T phase is set to zero as a reference. The inset schematically shows an interstitial Hf atom intercalated within a void (purple polyhedron) formed by surrounding six Hf and eight O atoms. (b) Energy variation along the polarization switching pathway of the O phase for different doping concentrations. (c) Polarization projected along the [111] crystallographic direction and switching barrier of the O and R phases. The results of 7%-strained R phase (hollow yellow circle) and experimental remanent polarization (dashed line) are extracted from Ref. [17].

In this Letter, we combine DFT and deep potential molecular dynamics (DPMD) simulations [21] to investigate how interstitial Hf doping reduces the coercive field in ferroelectric HfO_2. We find that interstitial Hf dopants diminish the energy difference between the polar orthorhombic $Pca2_1$ phase and the intermediate tetragonal $P4_2/nmc$ phase, lowering the switching barrier and coercive field. Unlike the R phase, which demands additional compressive strains for polarization, the $Pca2_1$ phase of $Hf_{1.03}O_2$, with a moderate doping concentration of 3%, already exhibits a low switching barrier and a high polarization. We propose that the $Pca2_1$ phase of HfO_2 with interstitial Hf defects better explains experimental observations. Large-scale MD simulations at finite temperatures with a DFT-derived machine learning force field demonstrate that 0.5% interstitial doping in $Pca2_1$ HfO_2 is enough to reduce the switching field significantly. Moreover, after a prepoling treatment during which interstitial dopants induce the formation of mobile domain walls, the switching field can drop below 1 MV/cm, comparable to experimental results. Further DFT calculations examining various interstitial dopants indicate a negative correlation between the switching barrier and dopant size, revealing several promising interstitial dopants that can lower the coercive field.

We start with an analysis of the phase stability of $Hf_{1+x}O_2$ with charge-neutral interstitial Hf dopants (Hf_i), considering the monoclinic (M) $P2_1/c$, polar orthorhombic (O) $Pca2_1$, tetragonal (T) $P4_2/nmc$, rhombohedral (R) $R3m$, and cubic (C) $Fm\bar{3}m$ phases. Two doping concentrations, 3.125% and 6.25% (abbreviated as 3% and 6%), are modeled by intercalating one and two excess Hf atoms within the hollow sites in a 96-atom $2\times2\times2$ supercell, respectively. See additional computational details in the Appendix [22–37]. As shown in Fig. 1(a), pristine HfO_2 polymorphs exhibit an inverse correlation between the thermodynamic stability and crystal symmetry. With increasing Hf_i concentration, the energies of these phases become closer, suggesting higher Hf_i formation energy in lower-symmetry M and O phases but lower in higher-symmetry C and R phases. Calculations assuming a charge state of Hf_i^{4+} predict a similar trend (Supplemental Material [38], Sec. I). This dependence is due to different effective void sizes in each phase [see the inset of Fig. 1(a)]. Specifically, the M and O phases have smaller voids due to alternating fourfold-coordinated (4C) and threefold-coordinated (3C) oxygen atoms, hindering Hf_i integration and resulting in higher formation energy.

Consistent with previous DFT results [17], our calculations show that, compared to the T phase, Hf_i doping destabilizes the lower-symmetry M and O phases while imposing minimal impact on the relative stability of the R phase. This suggests that the R phase would become energetically more favorable than the O phase above a critical Hf_i concentration, if it remains stable. However, the Hf_i-doped R phase is nonpolar, requiring a (111) in-plane compressive strain to achieve a polarized R phase. Using a 36-atom hexagonal supercell with a 7% out-of-plane tensile strain and an excess Hf atom, Wang *et al.* reported a polarized R-$Hf_{1.08}O_2$ with a low switching barrier of 7.6 meV/atom [17]. Notably, such a high strain state should correspond to a large out-of-plane interplanar spacing, $d_{111} = 3.11$ Å. This does not align with the experimental XRD data of $Hf_{1+x}O_2$ films, which shows a (111) peak at $2\theta = 30.1°$, indicating only a 0.1° shift compared to the stoichiometric O phase (with $d_{111} = 2.96$ Å, see Supplemental Material [38], Sec. II).

In contrast to the R phase, the O phase is inherently polar and does not depend on applied strain for polarization. The ferroelectric switching barrier in the O phase can be estimated from the energy difference between the T phase and O phase ($\Delta E = E^T - E^O$) [11]. As illustrated in Fig. 1(a), interstitial doping elevates the energy of the O phase relative to the T phase, thereby reducing ΔE. Figure 1(b) plots the NEB energy variation along the switching pathway in the O phase for different doping concentrations. The switching barrier

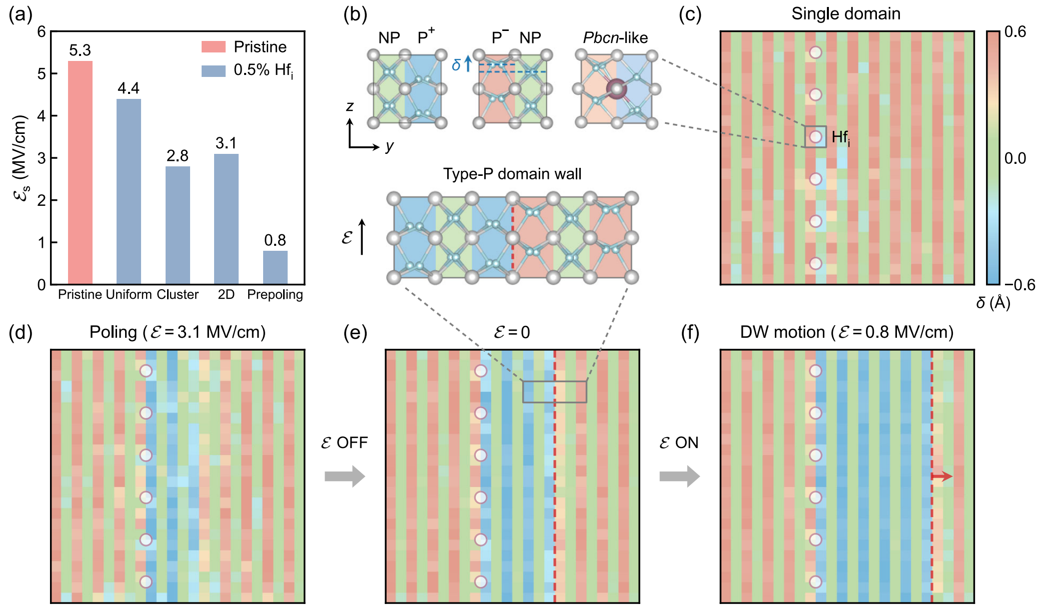

FIG. 2. Interstitial Hf dopants promoted polarization reversal at elevated temperatures. (a) Switching fields ($\mathcal{E}_s$) of pristine and interstitial-doped HfO_2 with various dopant distributions. (b) Alternately arranged nonpolar (NP) and polar (P^-/P^+) oxygen atoms in a $Pca2_1$ unit cell. The P^- oxygen atoms exhibit a positive local displacement (δ) of 0.54 Å. Distributions of δ in a $12 \times 12 \times 12$ supercell in the presence of two-dimensional-confined interstitial Hf dopants (denoted by hollow circles) between P^- and NP layers without an applied electric field (c), under poling at $\mathcal{E} = 3.1$ MV/cm (d), with the electric field turned off (e), and under subsequently poling at $\mathcal{E} = 0.8$ MV/cm (f). The left inset of (c) shows the local *Pbcn*-like structure surrounding an interstitial Hf. The top inset of (e) displays the atomic structure of a mobile type-P domain wall [46].

decreases drastically from 28 meV/atom in pristine HfO_2 to 12.3 meV/atom in $Hf_{1.03}O_2$, and further drops to 7.5 meV/atom in $Hf_{1.06}O_2$.

As summarized in Fig. 1(c), for the *O* phase, both the switching barrier and polarization decrease with increasing Hf_i concentration. This reduction in polarization is attributed to the diminished local displacements of polar oxygen atoms surrounding Hf_i. Further increasing Hf_i concentration destabilizes the *O* phase, causing it to transform into a *Pbcn*-like structure during DFT geometry relaxation. Importantly, *O*-$Hf_{1.06}O_2$, with a lower Hf_i concentration, exhibits a switching barrier (7.5 meV/atom) comparable to that of 7%-strained *R*-$Hf_{1.08}O_2$. It also features a higher spontaneous polarization along the [111] direction, matching closely to the experimental value. Moreover, we find that the diffraction pattern from mixed orientations of the $Pca2_1$ phase can produce (210) reflection spots, which were previously considered unique to the *R* phase (Supplemental Material [38], Sec. II). Although large local strains in polycrystalline thin films cannot be ruled out, the $Pca2_1$ phase with moderate interstitial Hf doping serves as a *minimal* model to explain experimental observations. We note that the Born effective charge (BEC) tensor of Hf_i exhibits all negative diagonal components of $\approx -2e$, indicating that its slight movement induces a change in polarization equivalent to the displacement of two negative elementary charges. This also means displacing the positively charged nucleus of Hf_i actually causes the associated negatively charged Wannier centers (WCs) to move in the same direction to a greater extent. This counterintuitive result is due to the fact that two WCs around Hf_i are less constrained by neighboring Hf—O bonds (Supplemental Material [38], Sec. III). Nevertheless, since the Hf_i dopant is strongly confined, it does not change the polarization switching mechanism identified with DFT-based NEB calculations.

Limited by computational cost, our DFT investigations focused on small supercells. This raises a legitimate question: how does the reduced energy difference between the *O* and *T* phases, seen in zero-kelvin DFT calculations, manifest in larger supercells at elevated temperatures that better represent the experimental sample conditions? To address this, we perform large-scale MD simulations at finite temperatures for an *O*-$Hf_{1.005}O_2$ supercell of 20 772 atoms, considering different Hf_i dopant distributions. The force field is a deep neural network-based model potential [15], which accurately reproduces various properties including the energy variation along the switching pathway in $Hf_{1+x}O_2$ (Supplemental Material [38], Sec. IV). All simulations are conducted at 400 K to facilitate the switching process on (sub)nanosecond timescales, thereby mitigating computational cost. We gauge the ease of switching by determining the lowest field strength ($\mathcal{E}_s$) that triggers polarization switching within 200 ps in MD simulations (see the comparison between $\mathcal{E}_s$ and $\mathcal{E}_c$ in Supplemental Material [38], Sec. V). As shown in Fig. 2(a), the switching field is 5.3 MV/cm for pristine single-domain HfO_2. Introducing uniformly distributed 0.5%

Hf_i dopants decreases $\mathcal{E}_s$ to 4.4 MV/cm. The local enrichment of Hf_i dopants further reduce $\mathcal{E}_s$: the clusterlike and two-dimensional (2D) distributions of Hf_i lead to $\mathcal{E}_s$ of 2.8 and 3.1 MV/cm, respectively.

We discover that a simple prepoling treatment can bring $\mathcal{E}_s$ to an even lower value of ≈0.8 MV/cm. The switching process extracted from MD simulations is presented in Figs. 2(c)–2(f), with the color scheme explained in Fig. 2(b). The starting configuration has 3C oxygen atoms displaced upward [polar (P^-)] relative to 4C oxygen atoms [nonpolar (NP)]. The 2D-confined Hf_i dopants are distributed uniformly within the xz plane between P^- and NP layers. A main impact of Hf_i is the slight downward displacement of 4C atoms [left inset of Fig. 2(c)]. Upon poling with an electric field of $\mathcal{E} = 3.1$ MV/cm, the Hf_i enriched layer facilitates the nucleation of 180° domain walls characterized by oppositely polarized 3C atoms, referred to as type-P walls [see Fig. 2(d)]. Locally, the type-P wall resembles a $Pbcn$ unit cell, consistent with DFT calculations showing a spontaneous transformation of the O phase to a $Pbcn$-like structure at high Hf_i concentration. We confirm that Hf_i dopants reduce the type-P domain-wall energy (Supplemental Material [38], Sec. VI). Consequently, polarization switching is driven by the motion of a type-P wall, while the other type-P wall is pinned by Hf_i dopants. Previous experimental and theoretical studies have revealed the role of defects in inducing nanodomain structures [47] and influencing domain wall dynamics [48] in prototypical ferroelectric $BaTiO_3$. When the external field is turned off, the mobile type-P wall remains stable. After prepoling, a much lower electric field of 0.8 MV/cm is sufficient to drive the domain-wall motion again. We note that the effect of prepoling remains robust for a more realistic inhomogeneous distribution of Hf_i dopants (Supplemental Material [38], Sec. V). The prepoling treatment described here can be interpreted as an activation process that facilitates the formation of domain walls in doped hafnia. Given that experimental studies have demonstrated the effective regulation of domain wall density in perovskite ferroelectrics with electric field poling [49], a similar approach could be beneficial for engineering the coercive field in hafnia.

The above results show that the value of ΔE, easily accessible through DFT calculations at the unit cell level, can indeed serve as a useful descriptor for $\mathcal{E}_c$. To identify more types of dopants for regulating $\mathcal{E}_c$ in ferroelectric HfO_2, we perform high-throughput DFT calculations covering diverse dopant atoms, X = Hf, Zr, Ti, La, Ta, Y, Nb, Sn, Ge, Si, Al, Ga, In, Sb, Mg, Ca, Cu, Zn, with a fixed concentration of 3%. As shown in Fig. 3(a), ΔE between the T and O phases with interstitial dopants (X_i) is plotted against the dopant atomic radius, revealing a clear negative correlation. Interstitial dopants with large atomic radii, such as Hf, Zr, and Ti, tend to reduce the ΔE, while smaller interstitial atoms such as Si, Ge, and Sn tend to increase ΔE, potentially leading to higher $\mathcal{E}_c$.

This negative correlation between ΔE and dopant size for interstitial doping contrasts sharply with substitutional

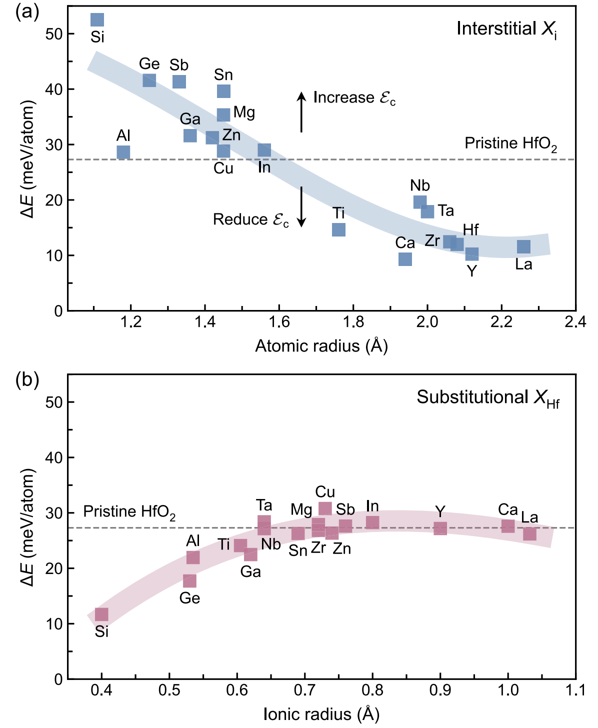

FIG. 3. Energy difference ($\Delta E = E^T - E^O$) between T-phase and O-phase HfO_2 with different dopants. (a) ΔE as a function of atomic radius for interstitial X_i doping. (b) ΔE as a function of ionic radius for substitutional X_{Hf} doping. The doping concentration is set to 3%. The value for pristine HfO_2 is denoted by a dashed line as a reference.

doping, where a volcanolike dependence (mostly a positive correlation) of ΔE on the ionic radius of the substitutional dopant was reported [11]. We further examine substitutional doping with atom X (X_{Hf}) and plot ΔE as a function of the ionic radius of X [see Fig. 3(b)]. Different from interstitial doping, the ΔE of HfO_2 under substitutional doping increases with dopant size, consistent with previous DFT results [11]. Notably, only a few small substitutional dopants, like Si_{Hf}, effectively lower ΔE. This has been attributed to the formation of stable sp^3 bonds between the substitutional Si dopant and neighboring oxygen atoms in the T phase [11].

To comprehend the diametrically opposing effects of Hf_i and Si_i on ΔE and $\mathcal{E}_c$, we analyze the bonding of interstitial atoms in the T and O phases of HfO_2. As depicted in Fig. 4, the intercalated atom is surrounded by eight oxygen atoms. We quantify the bonding strength of an interstitial dopant based on the bond-valence conservation principle [50,51]. According to this principle, each atom i has a preferred atomic valence $V_{0,i}$, which is often the nominal oxidation state of the atom (e.g., +4 for Hf). The actual atomic valence V_i is obtained by summing the individual bond valence (V_{ij}) for bonds between the atom and its neighbors (j), $V_i = \sum_j V_{ij}$. The deviation of V_i from $V_{0,i}$ is a measure of the stability of a given configuration. The bond

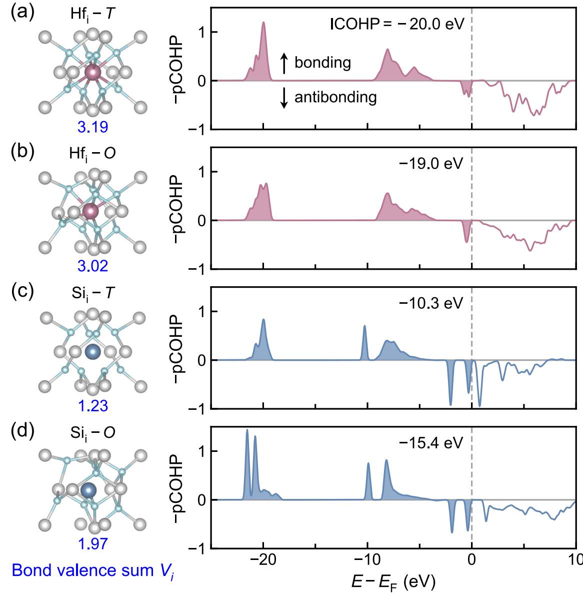

FIG. 4. Bonding analysis for interstitial Hf and Si with their neighboring oxygen atoms. (a) Hf_i in T phase. (b) Hf_i in O phase. (c) Si_i in T phase. (d) Si_i in O phase. The left panel shows the local atomic structure surrounding the interstitial atom, with the bond valence sum $V_i = \sum_j \exp[(R_o - R_{ij})/B]$ highlighted at the bottom. The Brown's empirical parameters $R_o = 1.923$ Å and $B = 0.375$ Å for Hf, and $R_o = 1.624$ Å and $B = 0.389$ Å for Si [52] are used in the bond valence calculation. The right panel shows the projected crystal orbital Hamilton population (pCOHP) averaged over eight oxygen–dopant pairs, labeled with the total integration of COHP (ICOHP).

valence for each oxygen-dopant pair is calculated as $V_{ij} = \exp[(R_o - R_{ij})/B]$, where R_{ij} is the bond length, R_o and B are Brown's empirical parameters [52]. The calculated V_i for Hf_i is 3.19 in the T phase and 3.02 in the O phase, indicating Hf_i in the T phase is more stable than that in the O phase. This is further supported by the projected crystal orbital Hamilton population (COHP) analysis. As shown in the right panel of Fig. 4, the total integration of COHP (ICOHP) for $Hf_i - O$ pairs is −20.0 and −19.0 eV in the T and O phases, respectively. The higher magnitude of ICOHP in the T phase confirms stronger bonding between Hf_i and oxygen atoms. Additionally, our DFT calculations of domain wall energy for a type-P wall with interstitial defects (Zr, Ca, Y, La) and the substitutional defect Si show significant reductions compared to the undoped case (Supplemental Material [38], Sec. VI). This supports the mechanism of dopant-promoted formation of mobile walls that reduce $\mathcal{E}_c$, consistent with high-throughput DFT calculations based on ΔE.

The difference between the energy of the T and O phases containing Hf_i ($E^T[Hf_i]$ and $E^O[Hf_i]$) can be directly related to the differences in the formation energy of Hf_i ($E_f[Hf_i]$) as follows:

$$\begin{aligned}\Delta E &= E^T[Hf_i] - E^O[Hf_i] \\ &= (E^T[Hf_i] - E_0^T - \mu_{Hf}) - (E^O[Hf_i] - E_0^O - \mu_{Hf}) \\ &\quad + E_0^T - E_0^O \\ &= E_f^T[Hf_i] - E_f^O[Hf_i] + \Delta E_0 = \Delta E_f[Hf_i] + \Delta E_0,\end{aligned}$$

where μ_{Hf} is the chemical potential of Hf and E_0 is the energy of the pristine crystal. The relatively stronger Hf_i—O bonding in the T phase suggests a lower formation energy of Hf_i than that in the O phase ($E_f^T[Hf_i] < E_f^O[Hf_i]$) [53], which is responsible for the reduced ΔE compared to the undoped value (ΔE_0). In the case of Si_i, the projected crystal orbital Hamilton population (pCOHP) curve reveals a stronger antibonding character, which is corroborated by the small values of V_i. Importantly, both the magnitudes of ICOHP and V_i are larger in the O phase than those in the T phase. This points to a lower formation energy of Si_i in the low-energy O phase, which will further increase the energy difference between T and O phases.

In summary, our investigations combining both zero-kelvin DFT calculations and large-scale MD simulations at finite temperatures establish the link between interstitial doping and coercive field in ferroelectric $Pca2_1$ HfO_2. Unit-cell-level DFT calculations act as a mean-field-like analysis, demonstrating that the coercive field reduction from interstitial Hf doping is due to the lower defect formation energy in the intermediate $P4_2/nmc$ phase. MD simulations, better representing experimental conditions, suggest that interstitial Hf dopants likely promote switching by forming mobile $Pbcn$-like domain walls. With prepoling, a switching field of < 1 MV/cm can drive polarization reversal within subnanoseconds. Finally, high-throughput DFT calculations reveal a negative correlation between the switching barrier and the size of the interstitial dopant. The comprehensive understanding of the interaction between interstitial dopants and domain wall dynamics in hafnia offers useful guidelines for optimizing the coercive field in this silicon-compatible ferroelectric oxide.

Acknowledgments—T. Z., L. M., and S. L. acknowledge the support from National Key R&D Program of China (Grant No. 2021YFA1202100), Natural Science Foundation of Zhejiang Province (2022XHSJJ006), National Natural Science Foundation of China (Grants No. 12361141821, No. 12074319), and Westlake Education Foundation. S. D. acknowledges the support from National Natural Science Foundation of China (Grant No. 22375015) and the open research fund of Songshan Lake Materials Laboratory (Grant No. 2022SLABFK02). The computational resource is provided by Westlake HPC Center.

[1] T. S. Böscke, J. Müller, D. Bräuhaus, U. Schröder, and U. Böttger, Ferroelectricity in hafnium oxide thin films, Appl. Phys. Lett. **99**, 102903 (2011).

[2] S. S. Cheema *et al.*, Enhanced ferroelectricity in ultrathin films grown directly on silicon, Nature (London) **580**, 478 (2020).

[3] U. Schroeder, M. H. Park, T. Mikolajick, and C. S. Hwang, The fundamentals and applications of ferroelectric HfO_2, Nat. Rev. Mater. **7**, 653 (2022).

[4] B. Noheda, P. Nukala, and M. Acuautla, Lessons from hafnium dioxide-based ferroelectrics, Nat. Mater. **22**, 562 (2023).

[5] U. Schroeder, E. Yurchuk, J. Müller, D. Martin, T. Schenk, P. Polakowski, C. Adelmann, M. I. Popovici, S. V. Kalinin, and T. Mikolajick, Impact of different dopants on the switching properties of ferroelectric hafnium oxide, Jpn. J. Appl. Phys. **53**, 08LE02 (2014).

[6] Y. Wei, P. Nukala, M. Salverda, S. Matzen, H. J. Zhao, J. Momand, A. S. Everhardt, G. Agnus, G. R. Blake, P. Lecoeur, B. J. Kooi, J. Íñiguez, B. Dkhil, and B. Noheda, A rhombohedral ferroelectric phase in epitaxially strained $Hf_{0.5}Zr_{0.5}O_2$ thin films, Nat. Mater. **17**, 1095 (2018).

[7] J. Lyu, I. Fina, R. Solanas, J. Fontcuberta, and F. Sánchez, Growth window of ferroelectric epitaxial $Hf_{0.5}Zr_{0.5}O_2$ thin films, ACS Appl. Electron. Mater. **1**, 220 (2019).

[8] S. Estandía, N. Dix, J. Gazquez, I. Fina, J. Lyu, M. F. Chisholm, J. Fontcuberta, and F. Sánchez, Engineering ferroelectric $Hf_{0.5}Zr_{0.5}O_2$ thin films by epitaxial stress, ACS Appl. Electron. Mater. **1**, 1449 (2019).

[9] T. Song, R. Bachelet, G. Saint-Girons, R. Solanas, I. Fina, and F. Sánchez, Epitaxial ferroelectric La-doped $Hf_{0.5}Zr_{0.5}O_2$ thin films, ACS Appl. Electron. Mater. **2**, 3221 (2020).

[10] Y. Qi and K. M. Rabe, Phase competition in HfO_2 with applied electric field from first principles, Phys. Rev. B **102**, 214108 (2020).

[11] H. Yang, H.-J. Lee, J. Jo, C. H. Kim, and J. H. Lee, Role of Si doping in reducing coercive fields for ferroelectric switching in HfO_2, Phys. Rev. Appl. **14**, 064012 (2020).

[12] W. Wei, G. Zhao, X. Zhan, W. Zhang, P. Sang, Q. Wang, L. Tai, Q. Luo, Y. Li, C. Li, and J. Chen, Switching pathway-dependent strain-effects on the ferroelectric properties and structural deformations in orthorhombic HfO_2, J. Appl. Phys. **131**, 154101 (2022).

[13] S. Zhou, J. Zhang, and A. M. Rappe, Strain-induced antipolar phase in hafnia stabilizes robust thin-film ferroelectricity, Sci. Adv. **8**, eadd5953 (2022).

[14] H. J. Zhao, Y. Fu, L. Yu, Y. Wang, Y. Yang, L. Bellaiche, and Y. Ma, Creating ferroelectricity in monoclinic $(HfO_2)_1/(CeO_2)_1$ superlattices, Phys. Rev. Lett. **132**, 256801 (2024).

[15] L. Ma, J. Wu, T. Zhu, Y. Huang, Q. Lu, and S. Liu, Ultrahigh oxygen ion mobility in ferroelectric hafnia, Phys. Rev. Lett. **131**, 256801 (2023).

[16] M. Falkowski, C. Künneth, R. Materlik, and A. Kersch, Unexpectedly large energy variations from dopant interactions in ferroelectric HfO_2 from high-throughput *ab initio* calculations, npj Comput. Mater. **4**, 73 (2018).

[17] Y. Wang, L. Tao, R. Guzman, Q. Luo, W. Zhou, Y. Yang, Y. Wei, Y. Liu, P. Jiang, Y. Chen, S. Lv, Y. Ding, W. Wei, T. Gong, Y. Wang, Q. Liu, S. Du, and M. Liu, A stable rhombohedral phase in ferroelectric $Hf(Zr)_{1+x}O_2$ capacitor with ultralow coercive field, Science **381**, 558 (2023).

[18] I. Fina and F. Sánchez, Epitaxial ferroelectric HfO_2 films: Growth, properties, and devices, ACS Appl. Electron. Mater. **3**, 1530 (2021).

[19] J. Wei, G. Xu, M. Huang, Y. Wu, W. Li, H. Xiang, and S. Chen, Intrinsic instability of rhombohedral $(Hf,Zr)O_2$ phases and endurance crisis of Hf-based ferroelectric devices, Preprint at Research Square, 10.21203/rs.3.rs-2634489/v1 (2023).

[20] T. Zhu, S. Deng, and S. Liu, Epitaxial ferroelectric hafnia stabilized by symmetry constraints, Phys. Rev. B **108**, L060102 (2023).

[21] L. Zhang, J. Han, H. Wang, R. Car, and W. E, Deep potential molecular dynamics: A scalable model with the accuracy of quantum mechanics, Phys. Rev. Lett. **120**, 143001 (2018).

[22] G. Kresse and J. Furthmüller, Efficient iterative schemes for *ab initio* total-energy calculations using a plane-wave basis set, Phys. Rev. B **54**, 11169 (1996).

[23] P. E. Blöchl, Projector augmented-wave method, Phys. Rev. B **50**, 17953 (1994).

[24] G. Kresse and D. Joubert, From ultrasoft pseudopotentials to the projector augmented-wave method, Phys. Rev. B **59**, 1758 (1999).

[25] J. P. Perdew, K. Burke, and M. Ernzerhof, Generalized gradient approximation made simple, Phys. Rev. Lett. **77**, 3865 (1996).

[26] J. Sun, A. Ruzsinszky, and J. P. Perdew, Strongly constrained and appropriately normed semilocal density functional, Phys. Rev. Lett. **115**, 036402 (2015).

[27] H. J. Monkhorst and J. D. Pack, Special points for Brillouin-zone integrations, Phys. Rev. B **13**, 5188 (1976).

[28] R. D. King-Smith and D. Vanderbilt, Theory of polarization of crystalline solids, Phys. Rev. B **47**, 1651 (1993).

[29] D. Vanderbilt and R. D. King-Smith, Electric polarization as a bulk quantity and its relation to surface charge, Phys. Rev. B **48**, 4442 (1993).

[30] D. Sheppard, P. Xiao, W. Chemelewski, D. D. Johnson, and G. Henkelman, A generalized solid-state nudged elastic band method, J. Chem. Phys. **136**, 074103 (2012).

[31] R. Dronskowski and P. E. Bloechl, Crystal orbital Hamilton populations (COHP): Energy-resolved visualization of chemical bonding in solids based on density-functional calculations, J. Phys. Chem. **97**, 8617 (1993).

[32] S. Maintz, V. Deringer, A. Tchougréeff, and R. Dronskowski, LOBSTER: A tool to extract chemical bonding from plane-wave based DFT, J. Comput. Chem. **37**, 1030 (2016).

[33] J. Wu, Y. Zhang, L. Zhang, and S. Liu, Deep learning of accurate force field of ferroelectric HfO_2, Phys. Rev. B **103**, 024108 (2021).

[34] J. Wu, J. Yang, L. Ma, L. Zhang, and S. Liu, Modular development of deep potential for complex solid solutions, Phys. Rev. B **107**, 144102 (2023).

[35] Origin of interstitial doping induced coercive field reduction in ferroelectric hafnia, https://bohrium.dp.tech/notebooks/63383664759.

[36] P. Umari and A. Pasquarello, *Ab initio* molecular dynamics in a finite homogeneous electric field, Phys. Rev. Lett. **89**, 157602 (2002).

[37] S. Liu, I. Grinberg, and A. M. Rappe, Intrinsic ferroelectric switching from first principles, Nature (London) **534**, 360 (2016).

[38] See Supplemental Material at http://link.aps.org/supplemental/10.1103/PhysRevLett.134.056802, which includes Refs. [17,22–26,35,37,39–45], for phase stability

under interstitial doping, simulation of x-ray and electron diffraction patterns, negative Born effective charges of interstitial hafnium, deep potential force field, domain wall dynamics revealed by DPMD simulations, and doping-induced mobile domain wall verified by DFT calculations.
[39] R. Ruh and P. W. R. Corfield, Crystal structure of monoclinic hafnia and comparison with monoclinic zirconia, J. Am. Ceram. Soc. **53**, 126 (1970).
[40] M. Hoffmann, U. Schroeder, T. Schenk, T. Shimizu, H. Funakubo, O. Sakata, D. Pohl, M. Drescher, C. Adelmann, R. Materlik, A. Kersch, and T. Mikolajick, Stabilizing the ferroelectric phase in doped hafnium oxide, J. Appl. Phys. **118**, 072006 (2015).
[41] I. MacLaren, T. Ras, M. MacKenzie, A. J. Craven, D. W. McComb, and S. D. Gendt, Texture, twinning, and metastable "tetragonal" phase in ultrathin films of HfO_2 on a Si substrate, J. Electrochem. Soc. **156**, G103 (2009).
[42] I. A. El-Shanshoury, V. A. Rudenko, and I. A. Ibrahim, Polymorphic behavior of thin evaporated films of zirconium and hafnium oxides, J. Am. Ceram. Soc. **53**, 264 (1970).
[43] W. Kohn and L. J. Sham, Self-consistent equations including exchange and correlation effects, Phys. Rev. **140**, A1133 (1965).
[44] K. Momma and F. Izumi, Vesta: A three-dimensional visualization system for electronic and structural analysis, J. Appl. Crystallogr. **41**, 653 (2008).
[45] S. M. Yang, J. Y. Jo, T. H. Kim, J.-G. Yoon, T. K. Song, H. N. Lee, Z. Marton, S. Park, Y. Jo, and T. W. Noh, ac dynamics of ferroelectric domains from an investigation of the frequency dependence of hysteresis loops, Phys. Rev. B **82**, 174125 (2010).
[46] J. Wu, J. Yang, Y. Sun, and S. Liu, Low-coercive-field ferroelectric hafnia with mobile domain walls, arXiv:2403.09426.
[47] W. Peng, J. Mun, Q. Xie, J. Chen, L. Wang, M. Kim, and T. W. Noh, Oxygen vacancy-induced topological nanodomains in ultrathin ferroelectric films, npj Quantum Mater. **6**, 48 (2021).
[48] A. Dhakane, T. Xie, D. E. Yilmaz, A. C. T. van Duin, B. G. Sumpter, and P. Ganesh, A graph dynamical neural network approach for decoding dynamical states in ferroelectrics, Carbon Trends **11**, 100264 (2023).
[49] C. Qiu, B. Wang, N. Zhang, S. Zhang, J. Liu, D. Walker, Y. Wang, H. Tian, T. R. Shrout, Z. Xu, L.-Q. Chen, and F. Li, Transparent ferroelectric crystals with ultrahigh piezoelectricity, Nature (London) **577**, 350 (2020).
[50] I. D. Brown, Recent developments in the methods and applications of the bond valence model, Chem. Rev. **109**, 6858 (2009).
[51] S. Liu, I. Grinberg, H. Takenaka, and A. M. Rappe, Reinterpretation of the bond-valence model with bond-order formalism: An improved bond-valence-based interatomic potential for $PbTiO_3$, Phys. Rev. B **88**, 104102 (2013).
[52] O. C. Gagné and F. C. Hawthorne, Comprehensive derivation of bond-valence parameters for ion pairs involving oxygen, Acta Crystallogr. Sect. B **71**, 562 (2015).
[53] J. Wei, L. Jiang, M. Huang, Y. Wu, and S. Chen, Intrinsic defect limit to the growth of orthorhombic HfO_2 and $(Hf,Zr)O_2$ with strong ferroelectricity: First-principles insights, Adv. Funct. Mater. **31**, 2104913 (2021).

End Matter

Method—All DFT calculations are carried out using the Vienna *ab initio* simulation package (VASP) [22] with the projector augmented-wave (PAW) method [23,24] and the Perdew-Burke-Ernzerhof (PBE) exchange correlation functional [25]. Our benchmark study confirmed that the lattice constants and relative phase stability predicted by PBE are comparable to results obtained with other density functionals, including SCAN [26]. The cut-off energy for the plane-wave basis is set to 600 eV. The Brillouin zones of the 12-atom pseudocubic unit cell and the $2 \times 2 \times 2$ supercell for doped systems are sampled by Γ-centered $4 \times 4 \times 4$ and $2 \times 2 \times 2$ Monkhorst-Pack [27] k-point meshes, respectively. All the structures are fully optimized until the atomic forces converge to 0.01 eV/Å. The polarization values are determined using the Berry phase method [28,29]. The polarization switching pathway is determined using the nudged elastic band (NEB) method [30]. The bond order analysis is performed with the crystal orbital Hamilton population (COHP) method [31] implemented in LOBSTER [32]. To investigate the ferroelectric switching in $Hf_{1+x}O_2$ at finite temperatures, we perform isobaric-isothermal ensemble (NPT) MD simulations using a deep neural network-based force field [33,34], with model accuracy verification and sample inputs available via an online notebook [35]. The electric fields are included in MD simulations using the "force method" [36,37], where an additional force $\mathcal{F}_i$ is added on the ion i according to $\mathcal{F}_i = Z_i^* \cdot \mathcal{E}$, with Z_i^* being the Born effective charge (BEC) tensor of ion i.